# Pulsed Thermal Shock Enables Deep Heteroatom Substitution and Substantial Reduction of Graphene

Kai Wang [1,*], Tao Jia [1], Xu Zhang [1], Yufang Ren [1], Fengxiao Hou [1,*], Yuexian Song [1], Xiaobin Zhong [1], Yangang Zhang [1], Yaohui Zhang [1], Junfei Liang [1,*] and Hua Wang [2,*]

[1] Key Laboratory of Shanxi Province for Solar Thermal Technology, School of Energy and Power Engineering, North University of China, Taiyuan 030051, China
[2] Key Laboratory of Bio-Inspired Smart Interfacial Science and Technology of Ministry of Education, School of Chemistry, Beihang University, Beijing 100191, China
* Correspondence: wangkai92@nuc.edu.cn (K.W.); mercatushou@outlook.com (F.H.); junfeiliang@buaa.edu.cn (J.L.); wanghua8651@buaa.edu.cn (H.W.)

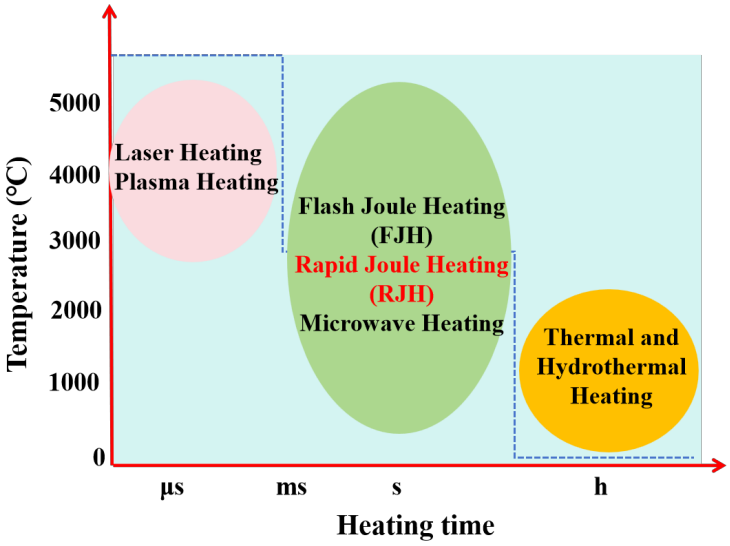


**Figure S1.** The temperature-time scale of the RJH method and other heating treatments.

## Pulsed Rapid Joule Heating Setup

The circuit diagram of the PRJH setup is shown in Figure S2. The PRJH setup delivers a maximum power output of 3500 W with a capacitance of 90 mF. The DC power supply operates at 3000 W (36 V×83 A), enabling an ultra-rapid joule heating temperature range of 400-3600 °C. The system achieves exceptional heating and cooling rates, reaching up to $10^5$ and $10^4$ °C/s, respectively. The vacuum reaction chamber serves as the operational environment for pulsed rapid joule heating reactions. The vacuum reaction chamber incorporates power wires, temperature sensor, sample stage, and multiple gas/vacuum ports, supplemented by an external vacuum pump, filtration flask assembly and with a Siemens programmable logic controller (PLC). The gas intake valve admits inert gases such as argon or nitrogen for atmosphere control. To maintain system integrity during gas infusion, operational protocols require maintaining a negative pressure of –0.02 MPa. Critical Safety

Note: This apparatus is strictly rated for negative-pressure operation only and is explicitly prohibited from use with flammable gas mixtures.

A quartz tube (10 mm ID, 1.5 mm wall thickness, 70 mm length) was loaded with reactant powder between two graphite plugs to form a sealed reaction assembly. The assembly was mounted in a pulse-heating holder, and the sample was mechanically compressed until the measured resistance reached 1-2 Ω.

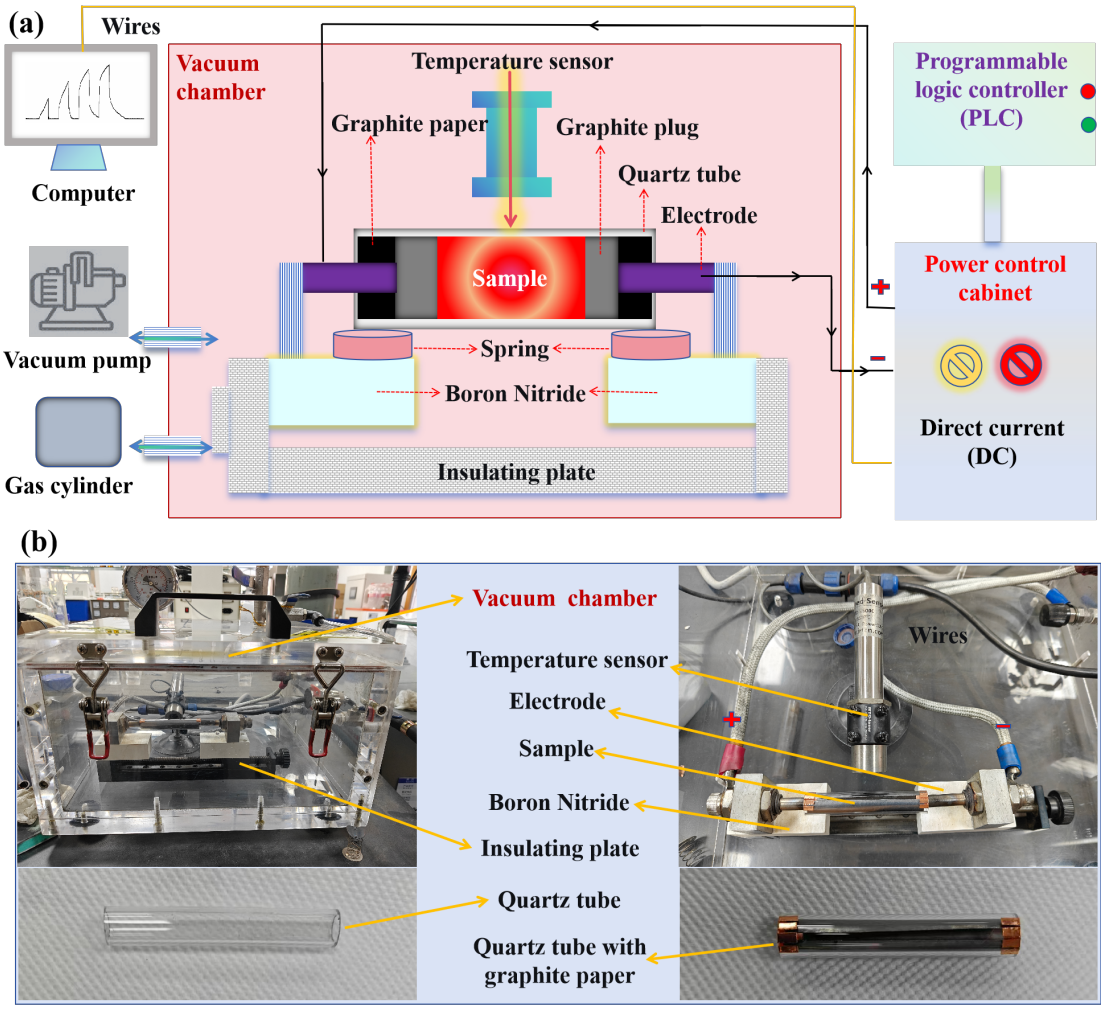


**Figure S2.** a) The circuit diagram of the dynamic pulsed rapid joule heating (PRJH) setup. b) The optical photo of the PRJH vacuum chamber.

**Table S1**. Experimental parameter design for PRJH process

| System | Voltage (V) | Current (A) | Number of pulses | Pulse duration (s) |
|---|---|---|---|---|
| GO→RGO | 30 | 50 | 4 | 10 |
| RGO/B→RGO-B | 20 | 45 | 10 | 3 |

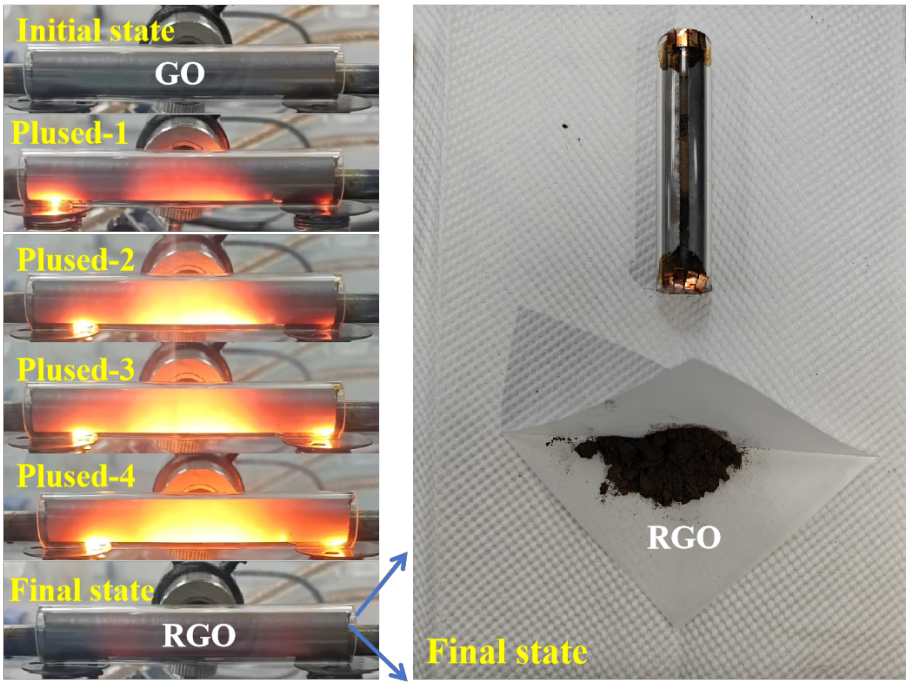


**Figure S3.** Sequential optical images capturing the PRJH process from GO to RGO over four consecutive pulses in quartz tube with graphite paper.

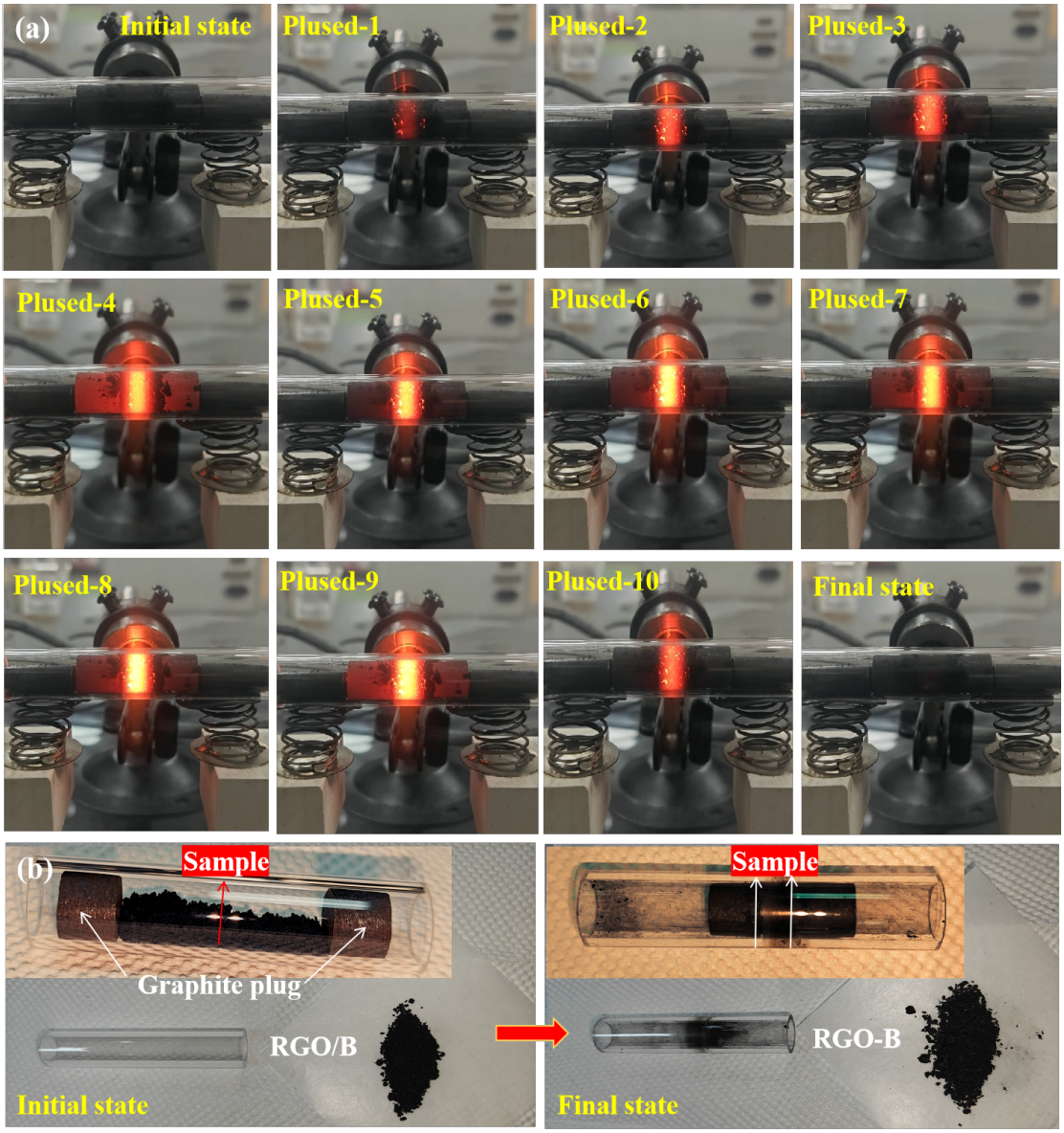


**Figure S4.** Sequential optical images capturing the PRJH process from RGO/B to RGO-B over ten consecutive pulses in quartz tube without graphite paper.

**Table S2**. Mass yield for different PRJH processes

| System | Mass of reactant (g) | Mass of product recovered (g) | Mass yield (%) |
|---|---|---|---|
| GO→RGO | 2.0 | 1.92 | 96 |
| RGO/B→RGO-B | 2.0 | 1.98 | 99 |

The mass yield can be obtained by equation 1:

Mass yield%=Mass of product recovered/Mass of reactant×100%

## Simulation Model Methods

The Vienna Ab Initio Package (VASP) code was employed to perform all the DFT calculations with periodic boundary condition, including binding energy calculation, geometry optimization and electronic structure characteristics. The GGA-PBE function in the projected augmented wave (PAW) method was used to describe the electron exchange correlation interaction, and the D3(BJ) method was used for dispersion correction to illustrate the weak interaction. In this work, to account for the diverse heteroatom doping configurations that may arise during practical pulse rapid Joule heating processes, three unit cell configurations of different atomic structures (RGO, RGO-B1, RGO-B2) was constructed. In the RGO-B1 configuration, a C atom adjacent to the O-bonded C in the O–C group is substituted by B atom, forming either B-C/B-C-O bonding environments. In the RGO-B2 configuration, the C atom directly bonded to O in the O–C group is replaced by B atom, resulting in the formation of B–O bonds. In the RGO-B3 configuration, a B atom is introduced adjacent to an existing B atom within the C lattice, forming B-B bonds instead of B-C/B-C-O or B-O bonding environments, as shown in Figure **S5**.

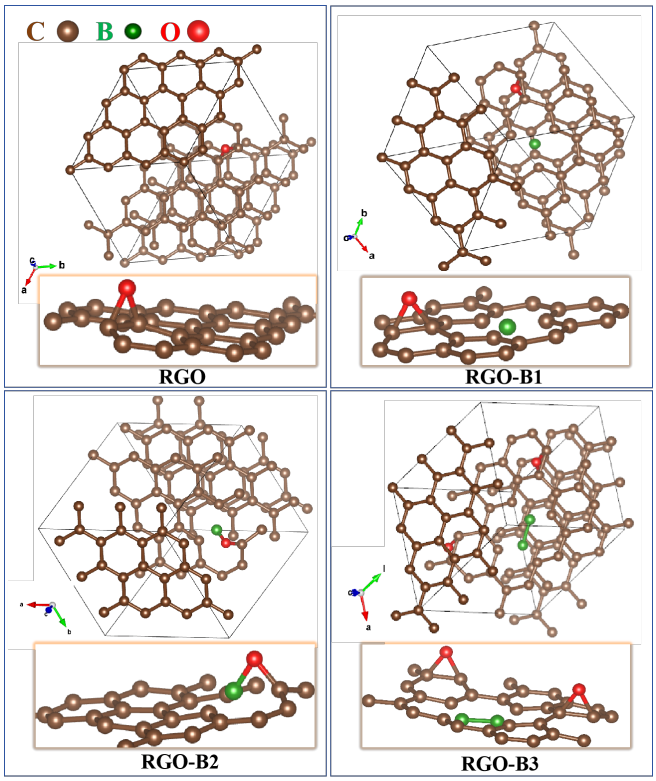


**Figure S5.** Unit cell configurations of different atomic structures.

**Table S3**. Binding energy of all configurations

| Configurations | Total (eV) | Surface (eV) | Li (eV) | Binding Energy (eV) |
|---|---|---|---|---|
| RGO-Li | -511.8536 | -508.6684 | -0.1018 | -3.0834 |
| RGO-B1-Li | -508.885 | -504.8611 | -0.1018 | -3.9221 |
| RGO-B2-Li | -509.6996 | -506.2369 | -0.1018 | -3.3609 |
| RGO-B3-Li | -503.9062 | -500.1342 | -0.1018 | -3.6702 |

**Table S4**. Energy barriers of the Li migration process

| Configurations | Energy Barrier (eV) |
|---|---|
| RGO-Li | 1.1743 |
| RGO-B1-Li | 0.0751 |
| RGO-B2-Li | 0.2407 |
| RGO-B3-Li | 0.1125 |

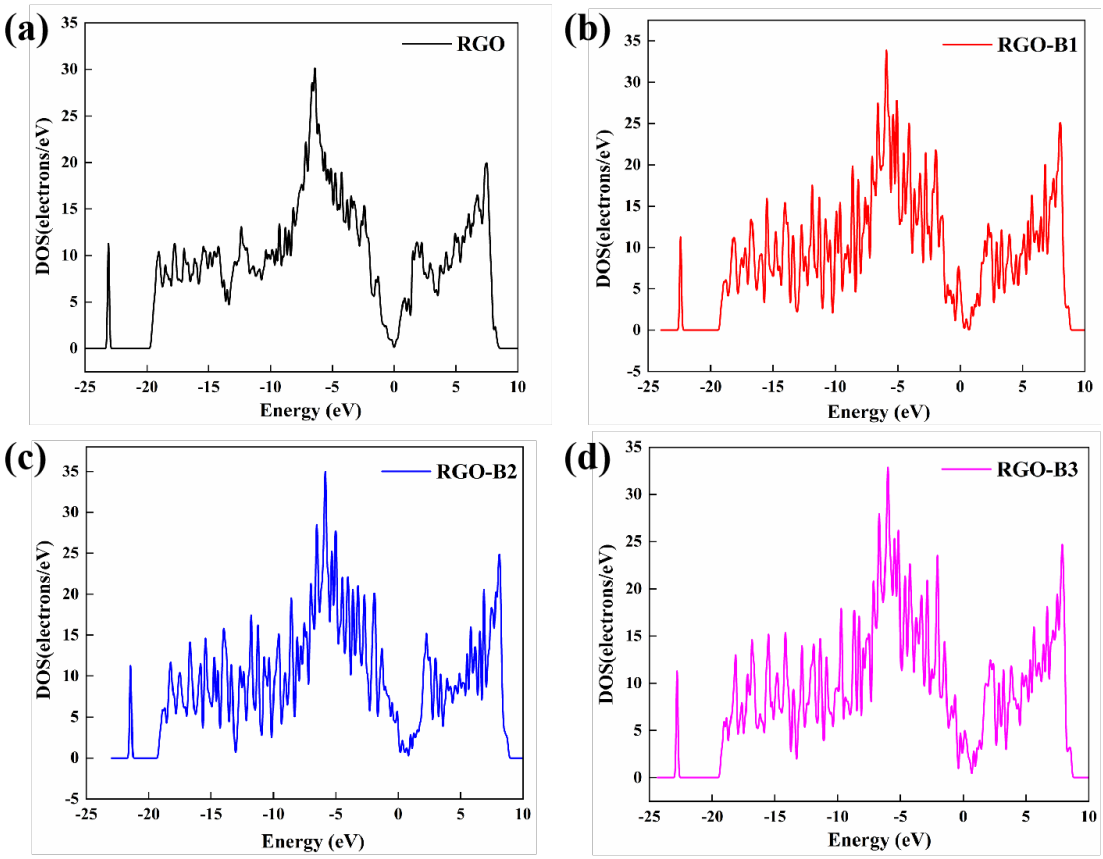


**Figure S6.** Density of states (DOS) for different structural configurations: a) RGO, b) RGO-B1, c) RGO-B2, d) RGO-B3.

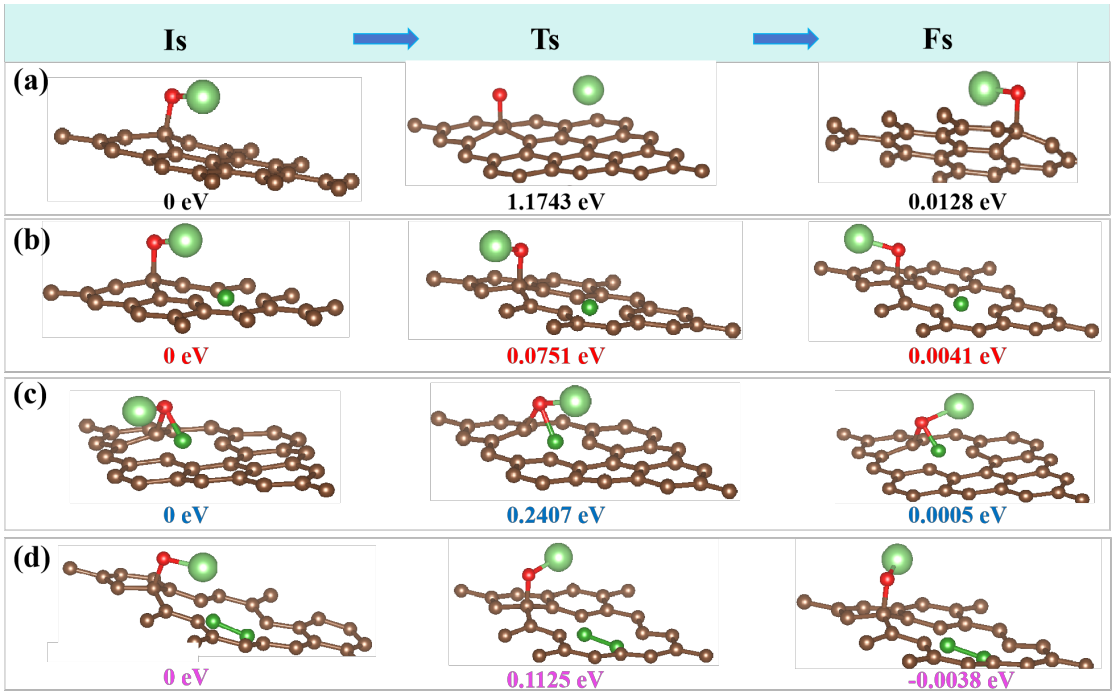


**Figure S7.** Energy barrier for Li migration of Initial, Transition and Final states: a) RGO, b) RGO-B1, c) RGO-B2, d) RGO-B3.

**Table S5.** Electron density difference distribution

| Atom | RGO-Li/e | | RGO-B1-Li/e | | RGO-B2-Li/e | | RGO-B3-Li/e | |
|---|---|---|---|---|---|---|---|---|
| | Origin | Binding | Origin | Binding | Origin | Binding | Origin | Binding |
| Li | - | 0.91 | - | 0.91 | - | 0.91 | - | 0.91 |
| O | -0.80 | -1.15 | -0.80 | -1.13 | -1.19 | -1.16 | -2.80 | -3.09 |
| C | 0.20 | 0.60 | 0.40 | 0.48 | 0.31 | -0.08 | 0.41 | 0.56 |
| B | - | - | 1.89 | 1.84 | 1.95 | 1.90 | 3.97 | 3.97 |
| B-B | - | - | - | - | - | - | 1.47 | 1.44 |

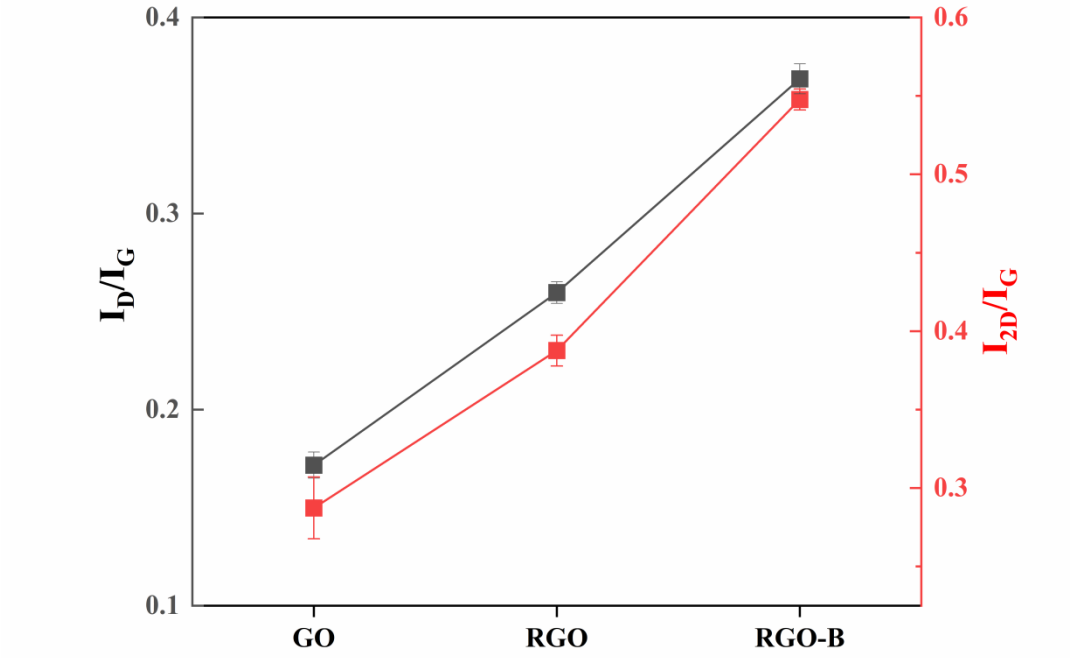


**Figure S8. $I_D/I_G$ and $I_{2D}/I_G$ ratios for GO, RGO and RGO-B.**

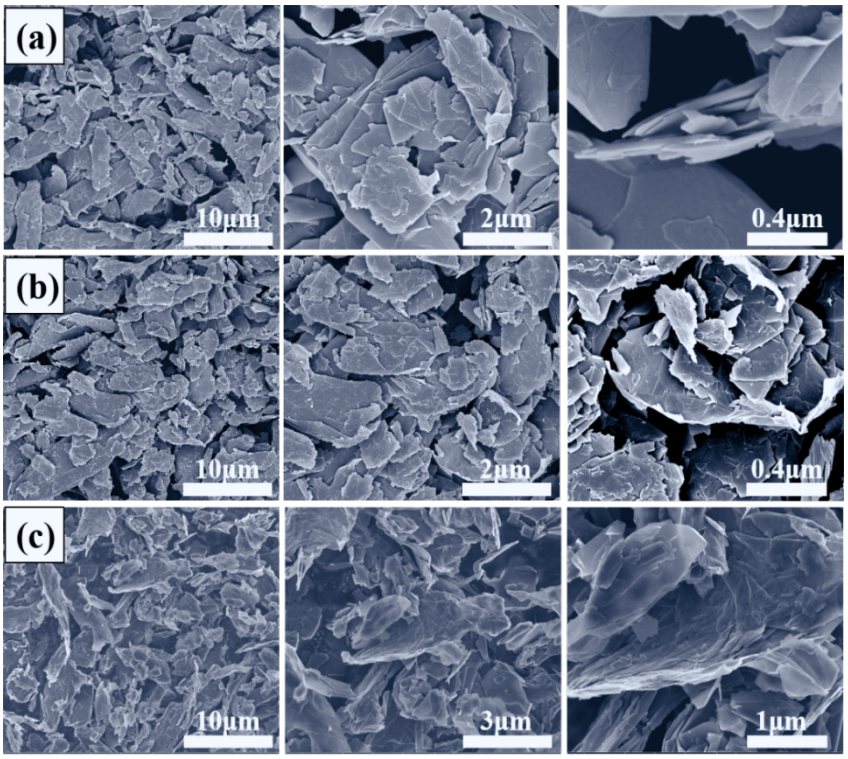


**Figure S9** SEM images at different magnifications: a) GO, b) RGO, c) RGO-B.

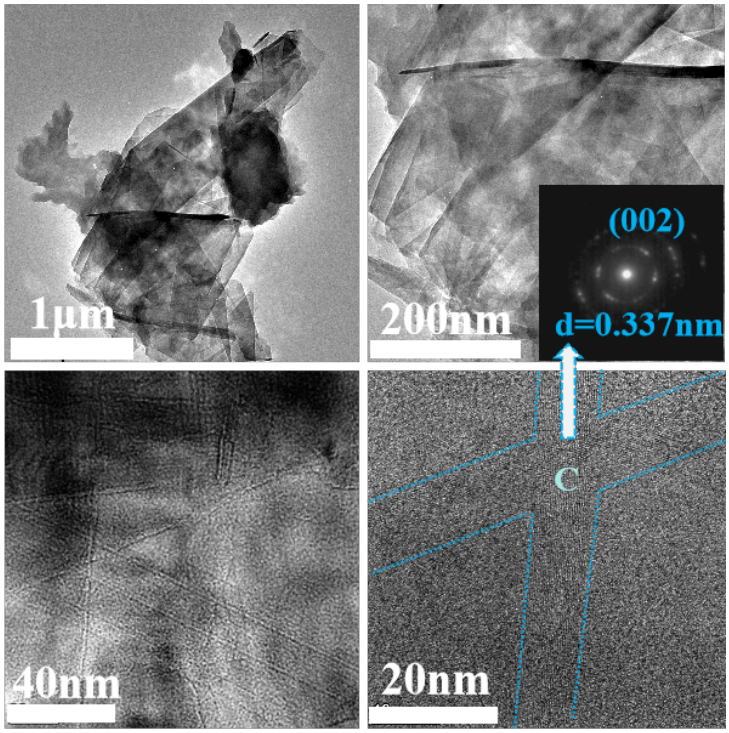


**Figure S10.** TEM and SAED images at different magnifications for GO sample.

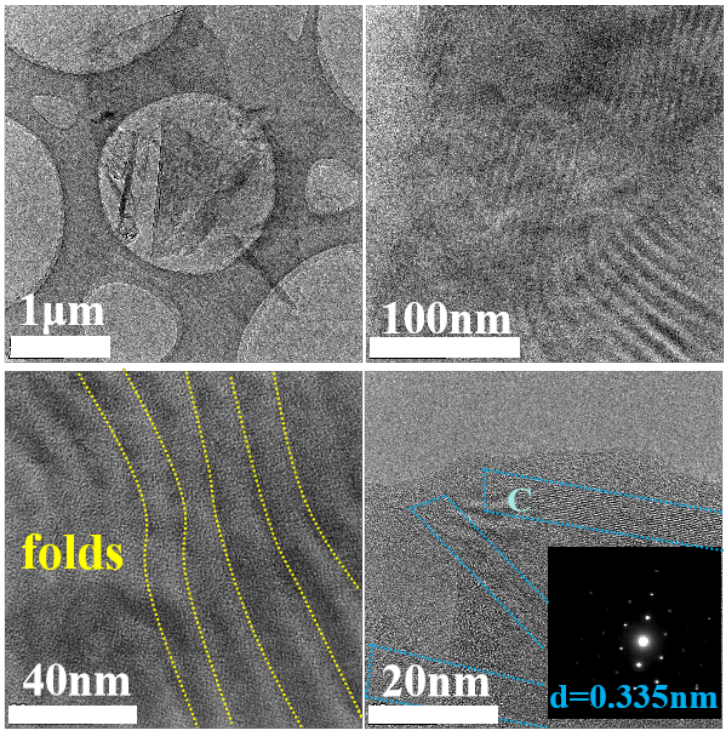


**Figure S11.** TEM and SAED images at different magnifications for RGO sample.

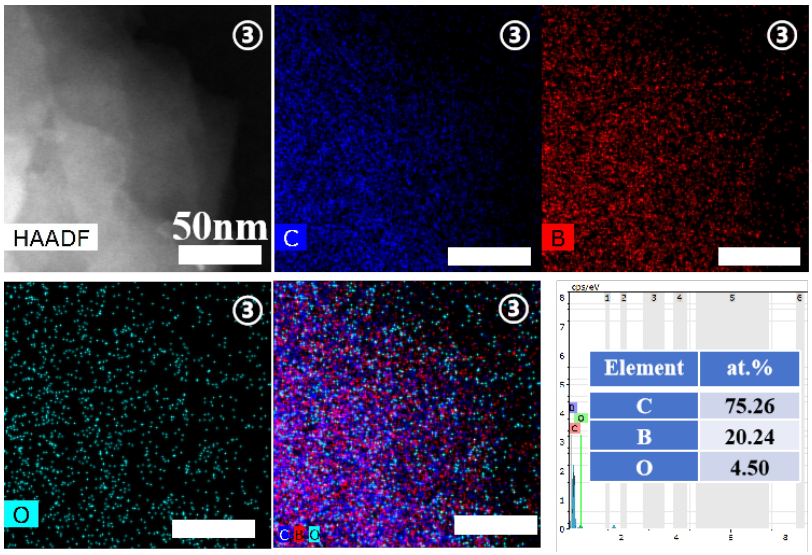


**Figure S12.** EDX elemental mapping and compositional analysis of local region ③ in RGO-B.

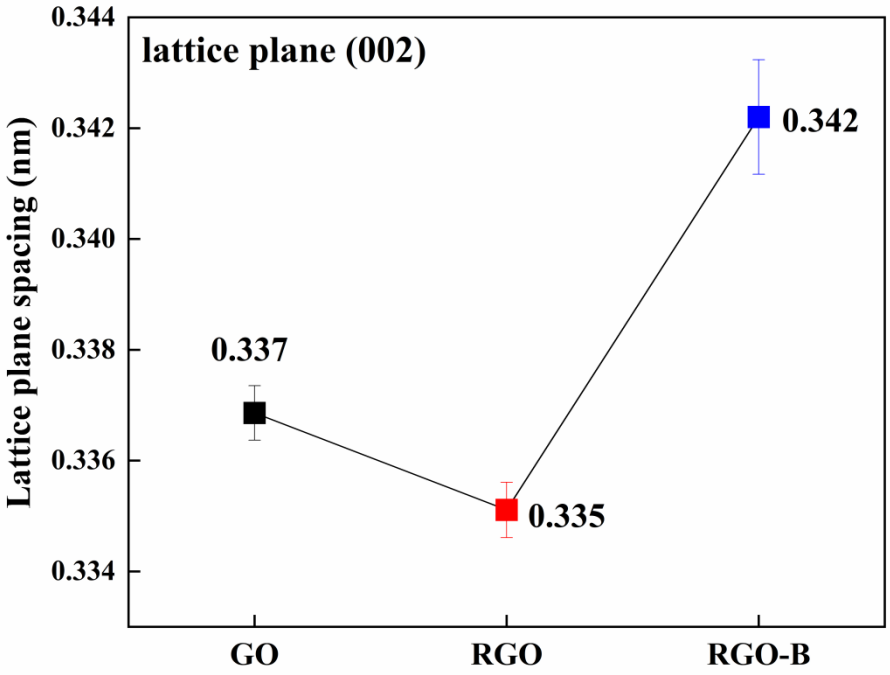


**Figure S13.** Variation in the (002) lattice plane d-spacing.

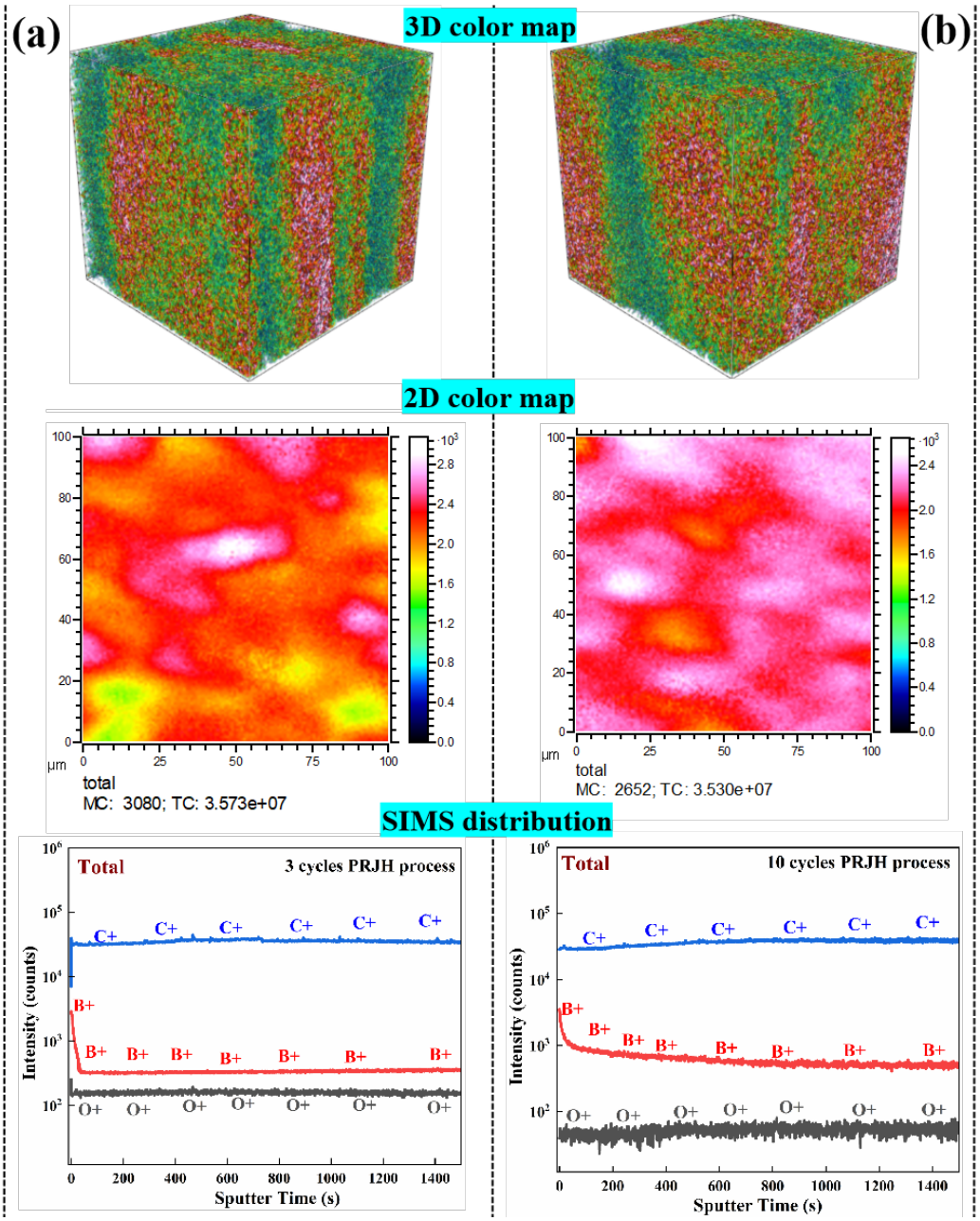


**Figure S14**. 2D and 3D color total maps and different element distributions for RGO-B a) 3 cycles PRJH and b) 10 cycles PRJH.

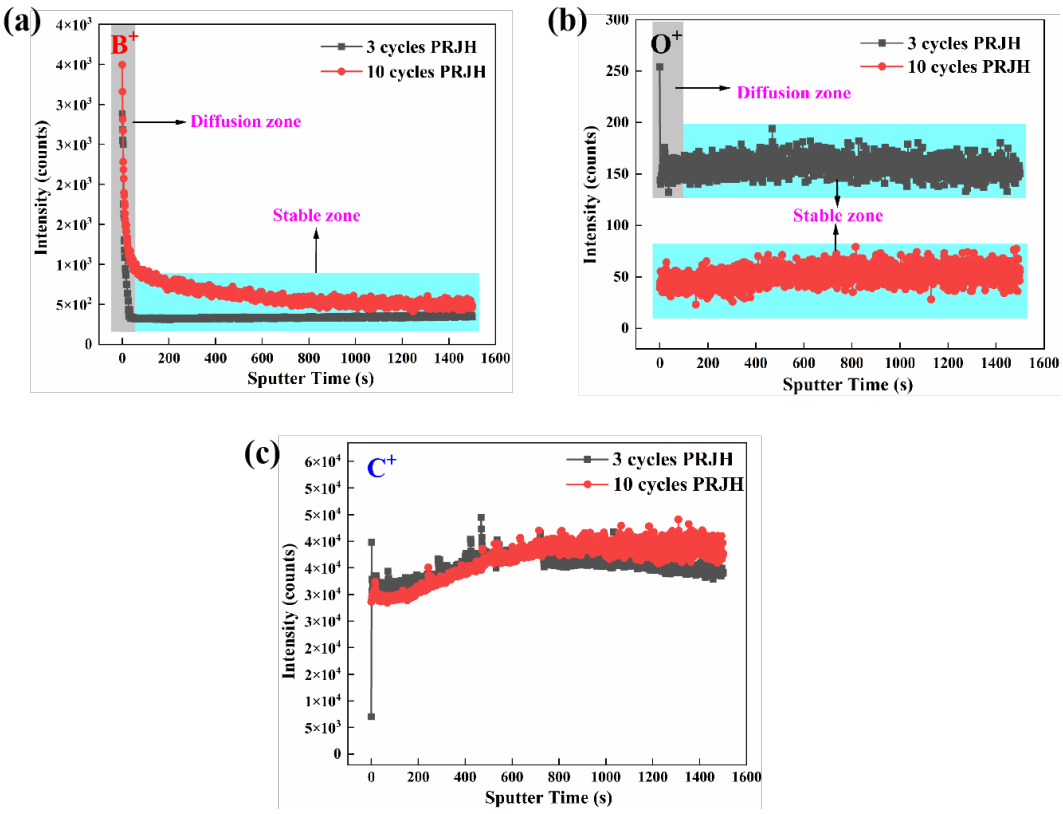


**Figure S15.** Atom distribution via SIMS Analysis of RGO-B samples at different cycles PRJH for a) B, b) O and c) C.

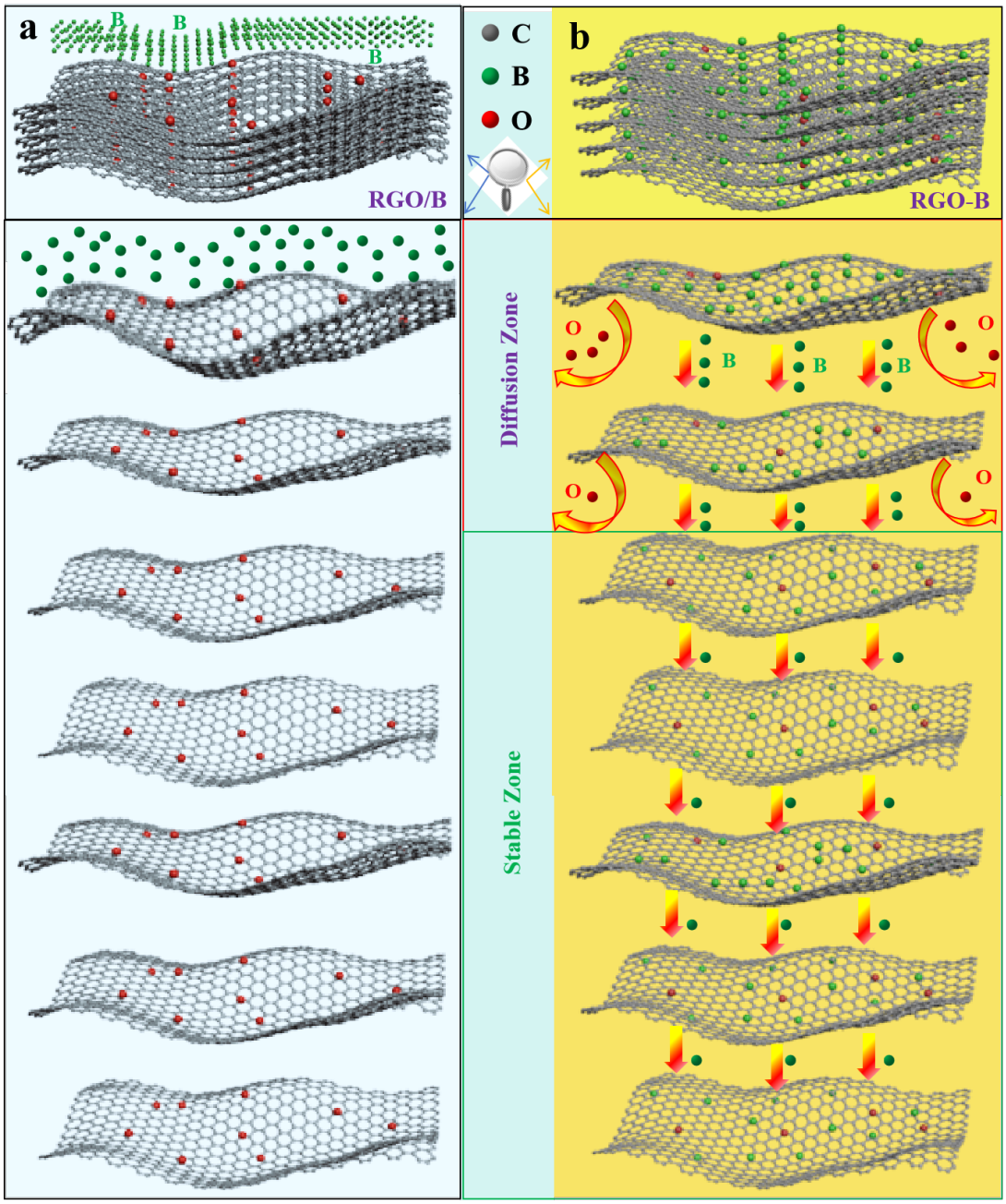


**Figure S16.** Schematic illustration of B and O elemental migration during the PRJH process for a) RGO/B and b) RGO-B samples.

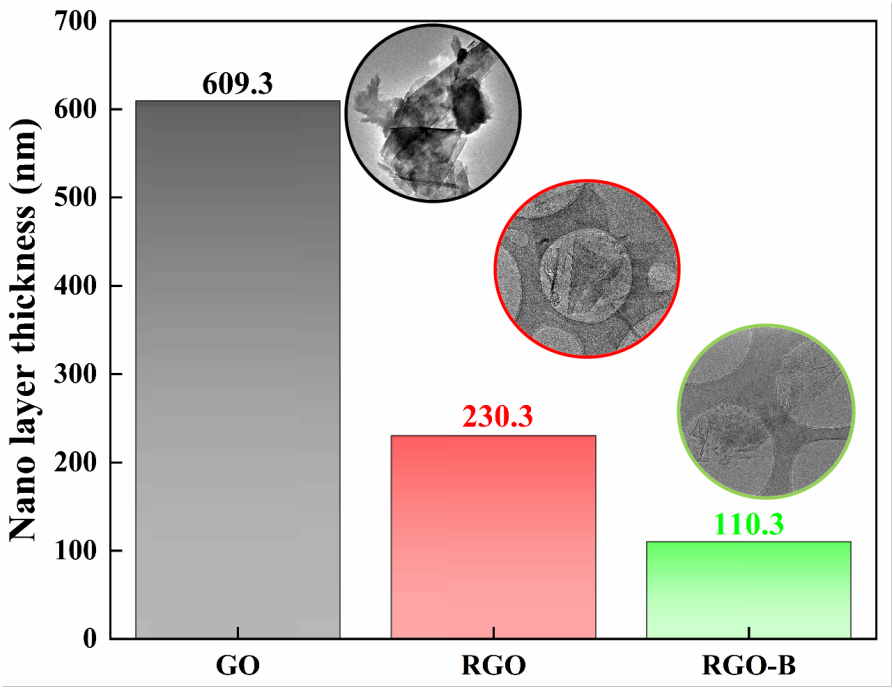


**Figure S17**. AFM Nano layer thickness variation for GO, RGO, RGO-B.

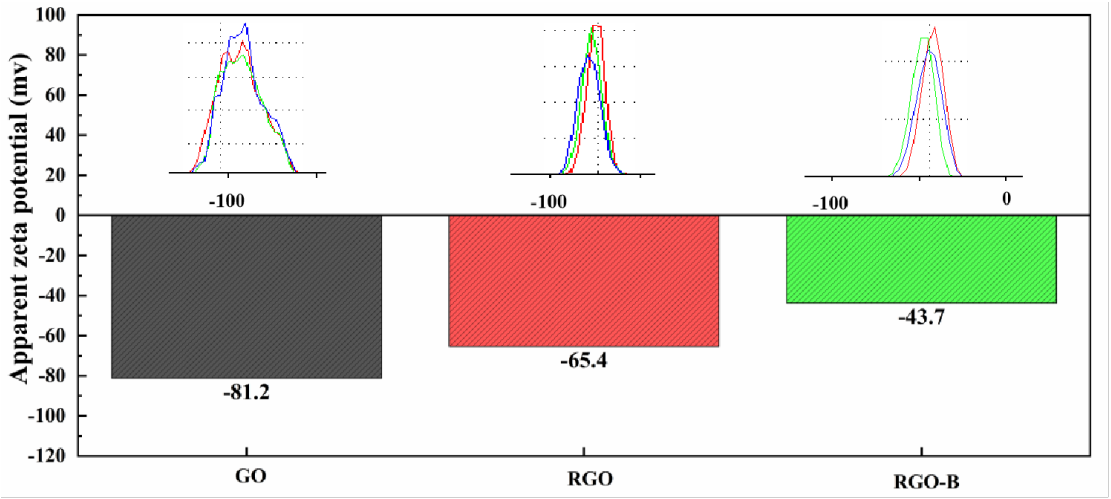


**Figure S18**. Zeta potential of GO, RGO, RGO-B.

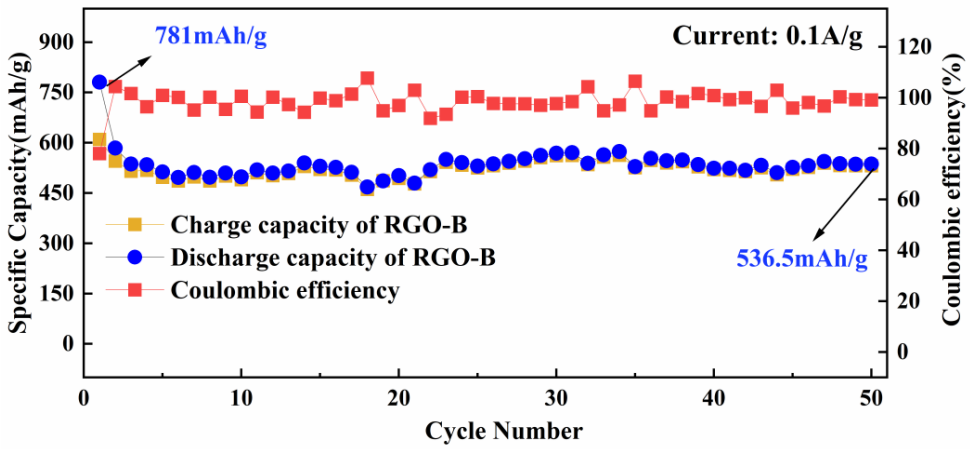


**Figure S19**. Cycling performance of RGO-B at a current density of 0.1 A/g.

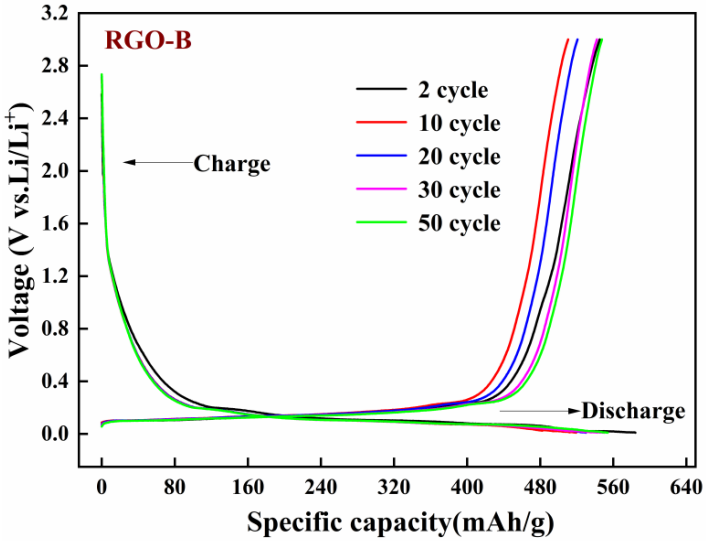


**Figure S20**. Charge-discharge profiles of RGO-B at a current density of 0.1 A/g.

**Electrochemical storage kinetic analysis**

To elucidate the exceptional rate capability and cycling stability of the electrode material, we further conducted lithium storage kinetic analysis on the RGO-B sample, with detailed results presented in Figure S19. The pseudocapacitive contribution was quantified using the following equations:

$$i = \alpha v^{b} \tag{S1}$$

$$logi = blogv + log\alpha \tag{S2}$$

where *a* and *b* represent the fitting parameter and adjustable parameter, respectively, and *i* denotes the current. Typically, the *b*-value of 0.5 indicates battery-like behavior, while $b \geqslant 1$ suggests dominant pseudocapacitive characteristics. When the *b*-value falls between 0.5 and 1, the electrode exhibits mixed behavior involving both battery-like and pseudocapacitive mechanisms. The fitting results for Peak A and Peak B yield *b*-values of 0.72 and 0.75, respectively, with both showing excellent linearity in the log*i*-log*v* plots. This confirms that the charge storage process in the RGO-B electrode is governed by a hybrid mechanism combining pseudocapacitive and diffusion-controlled processes. The pseudocapacitive contribution in this kinetic process can be quantified using the following equations:

$$i(V) = k_1 v + k_2 v^{1/2} \tag{S3}$$

$$i(V)/v^{1/2} = k_1 v^{1/2} + k_2 \tag{S4}$$

Where $i(V)$, $k_1 v$ and $k_2 v^{1/2}$ represent the total current response, capacitive, and diffusion control process, respectively. The pseudocapacitive contribution of the RGO-B electrode increased from 44.2% to 86.8 % with the rise in scan rates from at 0.1 mV/s to 1.0 mV/s. The pseudocapacitive contribution results reveal the dominant role of capacitive behavior and the fast $Li^+$ insertion/extraction characteristics of the capacitive storage mechanism. This enhanced performance can be primarily attributed to the deep penetration of B atoms into the RGO matrix under pulsed rapid Joule heating, where the formed B–C/B-C-O bonds significantly improve the electrical conductivity, increase active sites, and enhance cycling stability under ultra-high rate conditions.

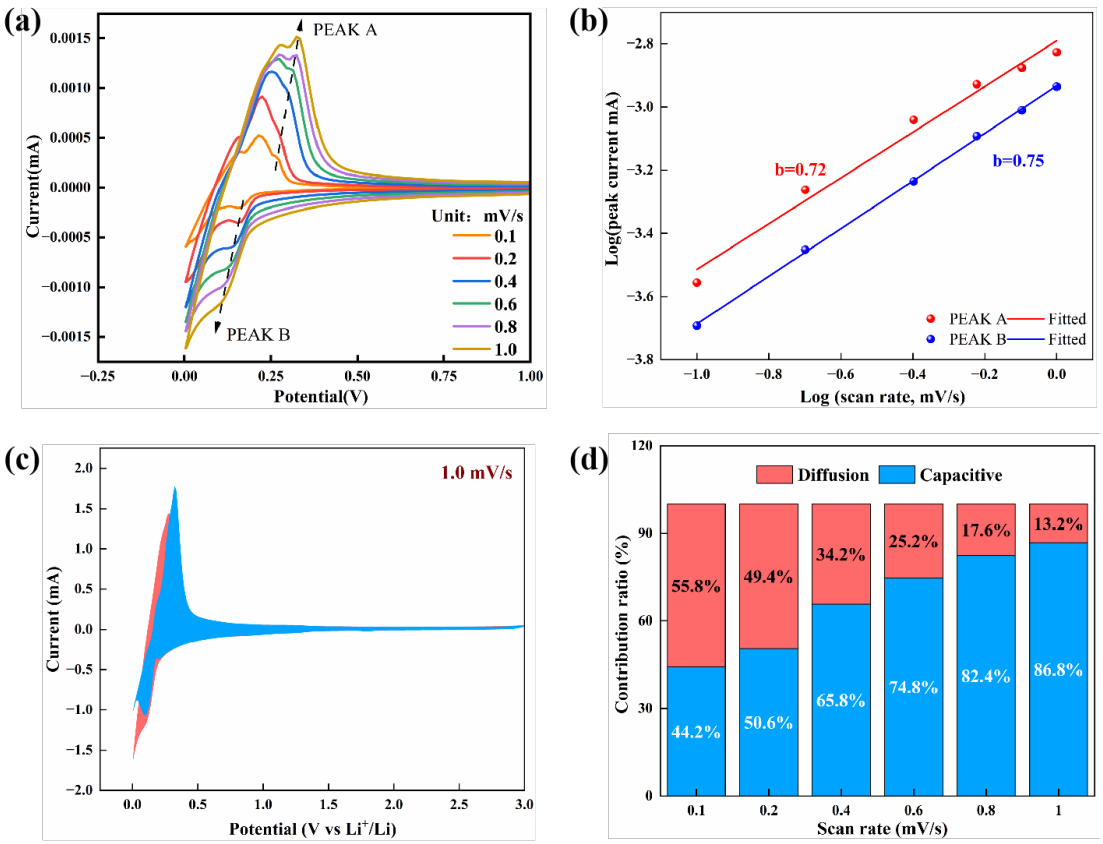


**Figure S21**. Electrochemical storage kinetic analysis of RGO-B composite. a) CV curves at different scan rates (0.1, 0.2, 0.4, 0.6, 0.8 and1.0 mV/s), b) the fitting lines between log i and log v, c) capacitive contribution in the CV curve (shaded region) at scan rate of 1.0 mV/s, and d) the ratio of capacitive and diffusive contributions at different scan rates.

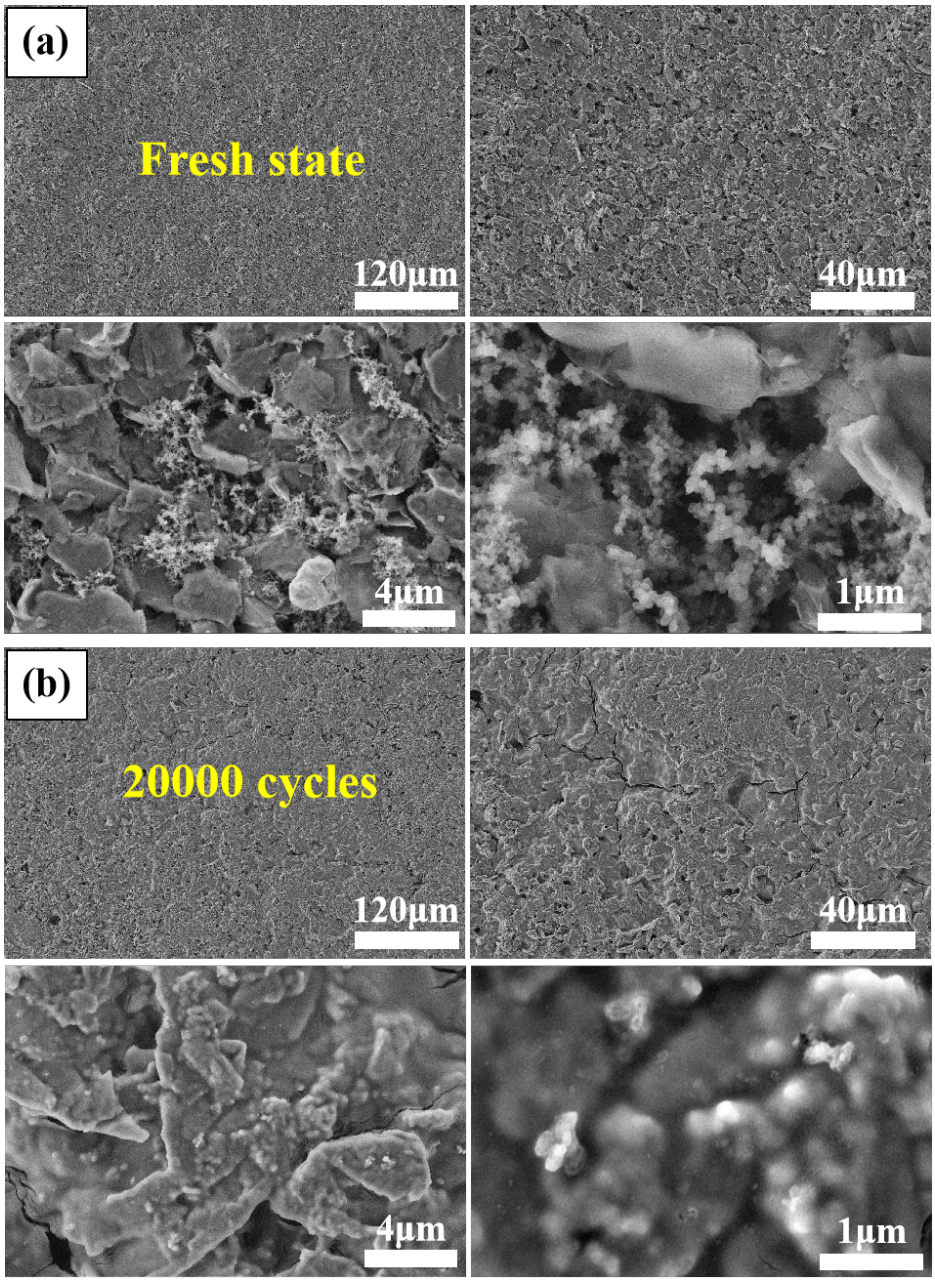


**Figure S22**. SEM images of the RGO-B electrode: a) Fresh state, b) After 20,000 cycles.

**Table S6**. Comparison for fast-charging LIBs of carbon-based anodes

| Samples | Preparation methods/ Time | Max capacity (mAh/g) | Final capacity (mAh/g)/ High c-rate | Capacity retention (%)/ Cycles | Ref. |
|---|---|---|---|---|---|
| B-graphene | Thermo-chemical method/～2h | 723 | 548/0.1A/g | 75.8%/30 | [43] |
| I-graphene | Hummer/～3h+ heating/～2h | 1690 | 1565/0.1A/ g | 92.6%/200 | [8] |
| P-mesoporous carbon | Chemical/58h+ heating/3h | 236.0 | 167/8C | 100.0%/20000 | [9] |
| N,B-graphene | Flash Joule heating/6.5s | 310 | ～300/0.2C | 96.7%/500 | [11] |
| B@RGO | Chemical/22h+ Chemical+Thermal annealing/13h | ～560 | 374/～5C | 66.8%/1000 | [15] |
| F-modified graphene | Arc-discharge method/～ | 452.7 | 412.0/5A/g | 91.0%/1000 | [17] |
| B-graphene | Heating/2h | 1549 | 1227/0.05A /g | 79.2%/30 | [36] |
| $BC_xO_{3-x}$/C | Annealing/2h | 591 | 446/0.2A/g | 75.5%/100 | [37] |
| B-graphene | Heating/3h | ～260 | 276/1.0A/g | 75.0%/1000 | [38] |
| B-graphite | Chemical/5h+ heating/2h | 355 | 325/0.18A/ g | 91.5%/50 | [44] |
| N-graphene/graphite | Hummer/～3h+ ultrasound/1h | ～200 | ～110/5C | 55.0%/2000 | [45] |
| B-porous C-PbO/Pb | Chemical/2h+ heating/1h | 538 | 330/0.2A/g | 61.3%/100 | [46] |
| Ag/B-RGO | Chemical/2h+ heating/4h | 1379 | 540/0.1A/g | 40.0%/100 | [47] |
| B-carbon nanotubes | Floating catalyst chemical vapor deposition/～ | ～500 | 548/0.1A/g | 109.6%/300 | [48] |
| B--graphene-LiVPO 4F@C | Sol-gel route/6.5h +heating/10h | 125.2 | 115.8/10C | 92.5%/300 | [49] |
| B, N-carbon flower | Chemical/10.5h+ annealing/1h | ～600 | 182.0/5C | 30.3%/3000 | [50] |
| Ordered/disordered hybrid C | Dual-shock Chemistry/1s | 208.6 | 169.1/10C | 81.1%/3000 | [51] |
| RGO-B | PRJH/～350s | 422.5<br>170.2 | 415.5/0.5C<br>115.9/13C | 98.3%/800<br>114.7%/20000 | This work |

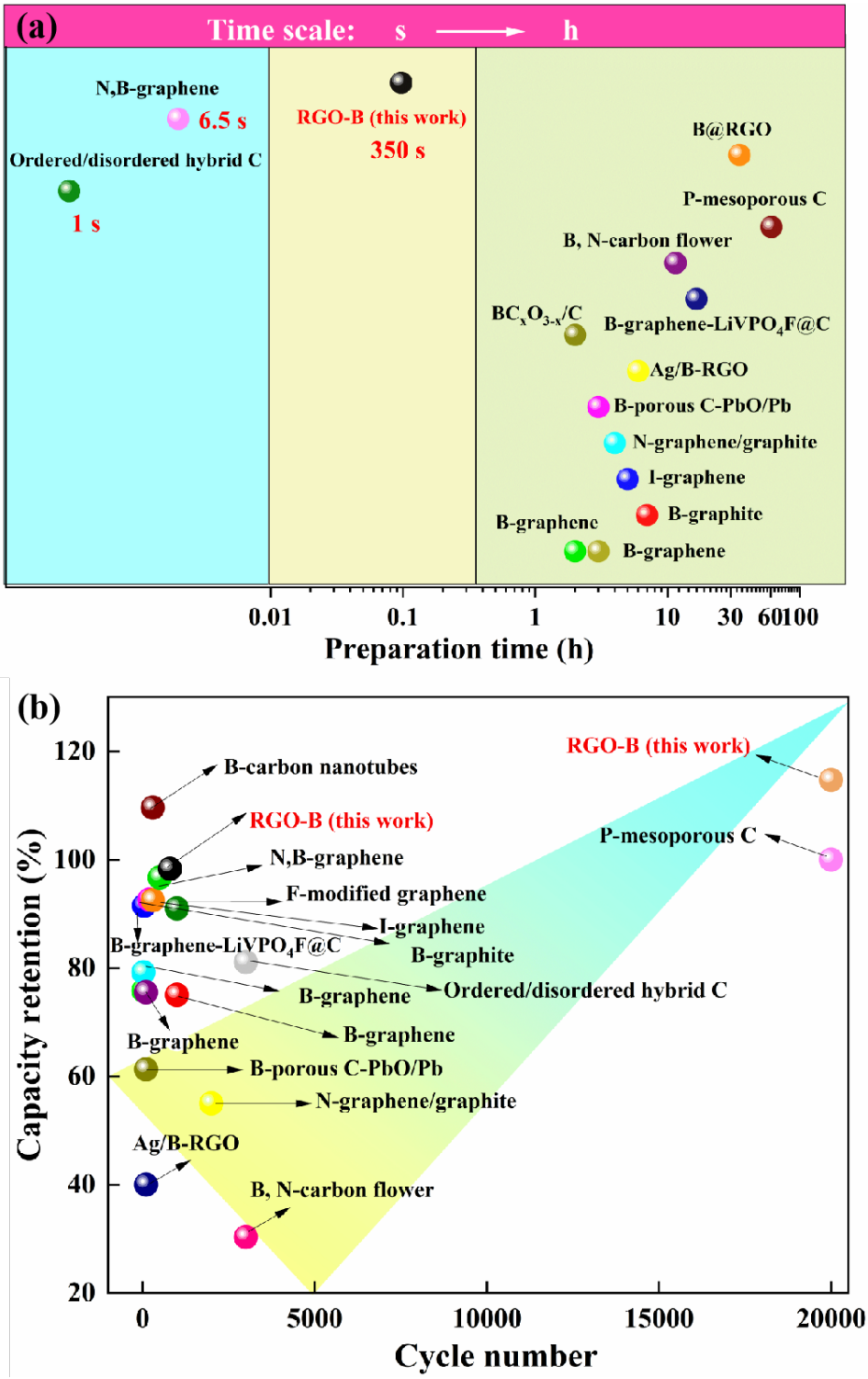


**Figure S23**. Comparison for fast-charging LIBs of carbon-based anodes from views of a) preparation time scale and b) capacity retention after cycling.